Diamond X-ray lens cubes with integrated aberration compensation

WENXIN WANG,[1,2,*] ![ID] RALPH DÖHRMANN,[1] STEPHAN BOTTA,[1] ANDERS MADSEN,[2] CHRISTIAN G. SCHROER,[1,3,4] ![ID] AND FRANK SEIBOTH[1] ![ID]

[1]*Center for X-Ray and Nano Science CXNS, Deutsches Elektronen-Synchrotron DESY, Notkestr. 85, 22607 Hamburg, Germany*
[2]*European X-Ray Free-Electron Laser Facility, Holzkoppel 4, 22869 Schenefeld, Germany*
[3]*Department Physik, Universität Hamburg, Luruper Chaussee 149, 22761 Hamburg, Germany*
[4]*Helmholtz Imaging, Deutsches Elektronen-Synchrotron DESY, Notkestr. 85, 22607 Hamburg, Germany*
*w.wang@desy.de

Abstract: Diamond is a highly suited material for radiation-resistant X-ray optics, particularly for 4th-generation synchrotron radiation sources with high brightness and X-ray free-electron laser (XFEL) facilities operating at high pulse energies. For various imaging applications, critical factors such as spatial resolution, bandwidth flexibility, and compact integration must be addressed in the design of focusing optics. However, the manufacturing process by laser ablation of diamond lenses often leads to residual aberrations and limitations in achievable spot sizes, posing challenges for high-resolution imaging applications. This work introduces an innovative concept of aberration-compensated X-ray lens cubes, composed of bi-concave, two-dimensional diamond lens plates with a 25 µm radius of curvature, fabricated by femtosecond laser ablation. A focal spot size of 52 nm × 51 nm was achieved at 14 keV, with wavefront errors strongly reduced across a wide photon energy range of 14 keV to 20 keV using multiple corrective phase plates. These results demonstrate the strong potential of our approach for nanoimaging applications, advancing high-resolution X-ray focusing capabilities for 4th-generation synchrotron radiation facilities and XFELs.

1. Introduction

Refractive X-ray lenses made from single-crystalline diamond have emerged as a promising alternative to beryllium (Be) for focusing X-ray beams at synchrotron radiation facilities and X-ray free-electron lasers (XFELs), particularly in 4th-generation light sources with significantly increased brightness. Diamond offers several advantages over Be, including higher refractive power [1], superior mechanical and radiation hardness [2], excellent thermal conductivity [3], high homogeneity [4,5], and greater fabrication shape flexibility, whereas Be can only be shaped by specific molds through press forming. These properties make diamond an ideal material for refractive X-ray optics, capable of withstanding high peak and average power densities in various applications. Short pulse laser ablation has drawn increasing attention during the last decades as an effective method for fabricating refractive diamond lenses [2,6,7]. However, these lenses often suffer from residual aberrations caused by the specific fabrication procedures, particularly following post-processing steps intended to reduce surface roughness [8,9]. Similar to Be compound refractive lenses (CRLs), a significant number of ablated diamond lenses introduce substantial wavefront distortions in the transmitted X-ray beam [8]. To address these distortions, phase plates – specialized optical components designed to compensate for wavefront errors – have been developed [10]. These optical elements correct phase shifts caused by deviations between

the ideal and fabricated lens shapes. Various materials and manufacturing techniques, both subtractive and additive, have been explored for producing phase plates to mitigate aberrations. They have been successfully implemented either as standalone optical components for Be CRLs [11–13] or as on-chip solutions for silicon nanofocusing lenses (NFLs) [14] across different photon energies. However, conventional phase plates are typically customized for specific lens assemblies based on prior characterization at a particular photon energy. The variation in X-ray beam convergence within a optically thick lens assembly across different photon energies restricts their applicability over a broad energy range [15].

In this work, we present a diamond lens assembly – denoted as a lens cube (LC) – with a build-in aberration correction that enables a broad working bandwidth. This lens system was specifically designed for high-resolution scanning X-ray microscopy at the PtyNAMi instrument [16] at P06 of PETRA III at DESY.

2. Fabrication of single diamond lens plates

The diamond lenses presented in this work were fabricated by femtosecond laser ablation. An Amplitude Satsuma HP^2 laser with a wavelength of 1032 nm and pulse duration of 285 fs is operated with a third harmonic frequency conversion unit at a wavelength of 343 nm and a pulse energy of up to 3 μJ at a repetition rate of 1 MHz. The pulse energy was adjusted to achieve a uniform material removal and minimal surface roughness. The lens shape was created by subsequently removing material layer by layer.

Figure 1(a) presents the sketch of a single diamond lens fabricated on a chemical vapor deposition (CVD) single-crystal diamond substrate. The substrate was pre-cut into a 3 mm × 3 mm plate with a thickness W ranging from 261 μm to 344 μm and an average of 295 μm. Both sides of the substrate were polished down to an arithmetic mean surface roughness of less than 30 nm. The laser pulses were focused on the surface of the substrate by an objective with a numerical aperture (NA) of 0.36, resulting in a spot size below 1 μm. The substrates were locally thinned down to a uniform thickness of 250 μm by ablation as pre-treatment. A solid paraboloid of revolution was removed layer by layer from the thinned down surface during the ablation process. This was achieved by a linear stage translation system. Subsequently, an identical paraboloid was removed on the opposite side to form a bi-concave lens of two aligned and opposed paraboloid structures. The targeted radius of curvature R of the lens is 25 μm, while the geometrical aperture D is 155 μm and the distance d between the two lens vertices is 10 μm to minimize absorption.
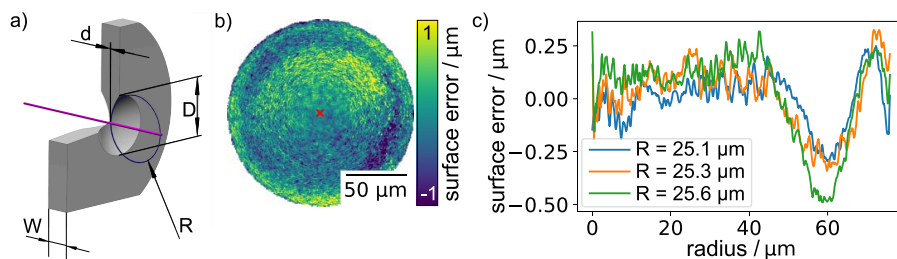

Fig. 1. Single diamond lens and its shape error measured by the LSM. a) Sketch of the geometry of a single diamond lens. b) 2D height error map (0.575 μm RMSE) of the single diamond lens with respect to a paraboloid fit with R = 25.1 μm. The measured geometric aperture is 156 μm. The red cross marks the center of the lens. c) Integrated radial error profile of three different single lenses. The blue line represents the lens in b), while the others have fitted R of 25.3 μm and 25.6 μm, respectively.

The in-lab metrology for the lens shape was implemented by a Keyence VK-X1100 confocal laser scanning microscope (LSM) using a 50× objective with NA = 0.95, which allows an initial

measurement of the ablated surface profile. The shape quality of an example single lens is shown in Fig. 1(b) with a root-mean-square surface error (RMSE) of 0.575 μm, which was evaluated by subtracting the best paraboloid fit to the measured data. The integrated radial error profiles around the center of three different lenses are plotted in Fig. 1(c), demonstrating the repeatability of lens fabrication. The RMSE for the radially integrated profile of the example lens is 0.361 μm while the radius of curvature R of the paraboloid fit is 25.1 μm.

3. Concept of the aberration-corrected X-ray lens cube

Each diamond lens substrate possesses a thickness of 295 μm on average, which is significantly less than the typical 1 mm to 2 mm thickness of standard commercial CRLs. Here, the lens substrate, typically a metallic Be disc, is encased in a coin packaging due to the material properties and constraints of the manufacturing process. In contrast, the robustness of diamond allows a close stacking of lens substrates without the need for an additional casing. Furthermore, the minimum achievable radius of curvature ($R = 50$ μm) and the lower density of the material restrict the refractive power of Be CRL, meaning that a larger number of Be CRLs are required to achieve an equivalent focal length compared to diamond lenses. Consequently, the spatial requirements to assemble a diamond lens stack are substantially reduced, leading to an optically thinner lens, capable of achieving a smaller X-ray focal spot size [1]. In addition, the integration into experimental setups can be simplified, enhancing the flexibility in potential applications.

In this context, the concept of a lens stack with integrated aberration compensation is proposed, as illustrated in Fig. 2. The assembly is named a lens cube (LC). The lenses mounted within this LC are inherently aligned, due to a consistent fabrication of each lens at a uniform location on its respective substrate. Together with identical substrate geometries, the manufacturing process is standardized across all lenses to ensure this uniformity. Additionally, the precise mounting rail (blue part in Fig. 2(a)) and spring structure (red part in Fig. 2(a)) incorporated in the LC assembly ensure accurate alignment of the substrates. The overall alignment accuracy for all the lenses and phase plates in the LC was within 5 μm. The center of each lens, that defines the optical axis, is located 6 mm away from the outer edges of the LC, as indicated in Fig. 2(a). The thickness C of the LC can be as thin as the combined thickness of all stacked diamond lens plates (no spacing). This design ensures that the LC can also be integrated into existing holders developed for mounting round 12 mm CRLs. Figure 2(c) illustrates a LC configuration containing 10 diamond lenses, which possess a focal length comparable to that of an assembly of 22 Be CRLs, shown for size comparison.

In the ideal case, a possible wavefront error can be corrected most precisely over the entire X-ray spectrum if each single lens has its own phase plate. This would ensure the optically thinnest possible element, minimizing propagation effects. However, each fabricated lens exhibits a shape error at the sub-micrometer scale, as depicted in Fig. 1(b), and fabricating a comparable shallow structure on a substrate presents challenges due to stringent accuracy requirements and the necessity of thinning down the substrate significantly in order to minimize absorption. Furthermore, the introduction of multiple additional substrates is likely to adversely impact the transmission rate of the X-ray beam due to the additional diamond material. An alternative approach involves stacking a small number of lenses and assessing the X-ray beam wavefront error induced by their cumulative shape error along the optical axis. The integrated aberration compensation is then achieved by incorporating one or more phase plates into the LC, depending on the number of lenses each phase plate is designed to correct. The phase plates are represented as pink slabs in Fig. 2(b).

Naturally, the location where the phase plate is fabricated corresponds precisely to the position of the lenses on their substrates. Various stacking configurations inside the LC offer flexibility in applications across a broad photon energy range. In addition, this concept can also be extended
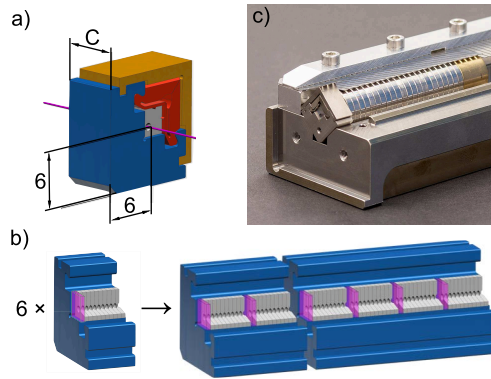
Fig. 2. Concept of the lens cube. a) Sketch of a single LC. b) Six LCs with 10 lenses are reconfigured into a combined LC stack, consisting of two LCs with 20 and 40 lenses, respectively. The pink slabs are the phase plates. c) A LC with 10 diamond lenses shown for comparison together with 22 Be CRLs of equivalent focal power. Both are positioned in a holder developed for mounting round 12 mm CRLs.

to a multi-LC configuration, as shown in Fig. 2(b), in order to adjust the number of lenses and thus the focal length.

4. Pre-characterization of lens stacks

4.1. Experimental setup

In this study, a total of 60 lenses were manufactured, and each set of 10 lenses was initially assembled into a LC. To design and fabricate the phase plates [11] capable of correcting the aberrations introduced by each set of lenses, the focused wavefield of each LC was characterized by at-wavelength metrology based on X-ray ptychography [17–19], offering the possibility of reconstructing the complex wavefield of the X-ray beam.

The ptychographic imaging experiments were conducted on the PtyNAMi instrument [16] at the nanoprobe endstation of beamline P06 of PETRA III at DESY. A photon energy of 9 keV was selected by a Si(111) monochromator to meet the working distance (WD) constraints of the PtyNAMi setup. The schematic configuration of the experiment can be seen in Fig. 3. Since the diamond substrates are almost transparent to X-rays, the geometrical aperture of the first upstream diamond lens does not function as an optical aperture. To address this, a circular tungsten pinhole, fabricated also by laser ablation, was placed roughly 5 mm upstream of the first lens to confine the illuminating X-ray beam. The pinhole diameter A is intentionally designed to be slightly smaller than the lens opening in order to restrict the X-ray beam size and ensure that the beam passes through the lenses without scattering from the edges. X-rays were focused by 10 diamond lenses with $R = 25$ μm, yielding a total lens thickness of 2.95 mm and a theoretical focal length f of 138.7 mm at 9 keV. A 30 μm diameter cleaning pinhole was placed between diamond lenses and the test sample close to the focal plane to further reduce the stray radiation. A Siemens star resolution test object made of 500 nm thick tantalum with 50 nm smallest features was placed in the vicinity of the focal plane. The object was scanned in a grid with 100 nm step size, covering an area of 4 μm × 4 μm in 40 × 40 steps with a dwell time of 0.1 s per scan point. A Dectris EIGER X 4M pixel detector [20] was used to record far-field diffraction patterns at a distance of 3195 mm downstream of the sample. The aperture size and distances in the experimental setup are summarized in Table 1. While the geometric aperture of the lenses is 156

µm, the size of the entrance pinhole *A* was chosen smaller on purpose to avoid illumination of the edge of the lenses.
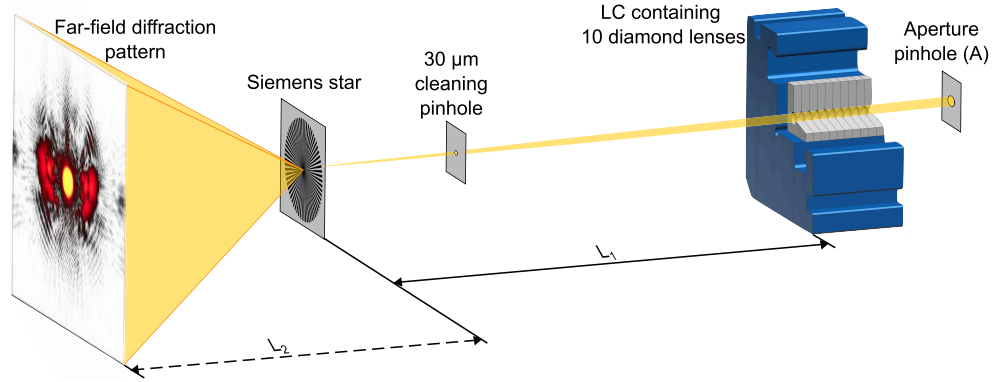

Fig. 3. Schematic of the ptychography experiment setup at P06 of PETRA III. For the pre-characterization, 6 sets of LCs with 10 diamond lenses each at 9 keV were used.

Table 1. Parameters of the characterization experiment for the single lens cubes at 9 keV and the combined lens cubes at 14, 17 and 20 keV. A is the aperture of the entrance pinhole (cf. Fig. 3).

E (keV)	No. of lenses	A (µm)	Phase plate	L_1 (mm)	L_2 (mm)
9	10	145	no	137	3195
14	60	120	no	49	3258
			yes	49	3249
17	60	120	no	75.6	3231
			yes	75.6	3232
20	60	120	no	106.7	3199
			yes	107.4	3200

4.2. Wavefront error of single lens cube

The complex wavefield created by each stack of 10 lenses at the object plane was obtained via ptychographic phase retrieval. By numerically propagating the complex wavefield using the Fresnel-Kirchhoff diffraction formula by 137 mm from the object plane to the exit of the lens stack along the optical axis, the wavefield at the exit plane of each lens stack was retrieved. The corresponding wavefront error for each lens stack was then obtained by fitting the first 6 Zernike polynomials for a circular aperture to correct for tilt, defocus and astigmatism, as depicted in Fig. 4(a) to (f), respectively. Due to the irregular distribution of errors near the boundary, we omitted the outer part of the error map extending beyond 60 µm distance from the center. Accordingly, the diameter of the entrance pinhole *A* was subsequently set to 120 µm in order to avoid illumination of these irregular lens areas. The wavefront error maps indicate that all the lens stacks exhibit a comparable shape error that is closely distributed in a rotationally symmetric manner, with some deviations in in Fig. 4(c) and (e). This demonstrates the repeatability of the lens fabrication, but also shows that individual characterization of each stack is still required. To obtain the average radial shape error profile for the lenses within each LC, the following procedure is employed: First, the two-dimensional wavefield error is integrated radially around the center of lens. The resulting value is then divided by the number of lenses in each LC.

Subsequently, the phase error ϵ_{phase} is converted into a shape error ϵ_{shape} by

$$\epsilon_{\text{shape}} = \frac{\epsilon_{\text{phase}}}{-k\delta_{\text{C}^*}(E)}, \qquad k = \frac{E}{\hbar c}, \tag{1}$$

where $\delta_{\text{C}^*}(E)$ is the refractive index decrement of diamond at photon energy E, k is the wavenumber, $\hbar$ is the reduced Planck constant and c is the speed of light in vacuum. These profiles are displayed as colored curves in Fig. 4(g), where the black curve depicts the mean radial shape error profile of a single lens averaged over the 6 characterized LCs. The RMSE of this mean profile is 0.06 µm versus 0.361 µm for an individual lens via LSM analysis. Although both these profiles and the height error map obtained via in-lab metrology shown in Fig. 1(c) demonstrate the repeatability of fabrication, some discrepancies are observed: Whereas Fig. 1(c) shows a flat error profile with large fluctuation up to 40 µm from the lens center, Fig. 4(g) shows a large slope over that range and a dip at a distance of 30 µm from the lens center. Furthermore, the pronounced valley in Fig. 1(c) near 60 µm distance from the lens center descends to −0.5 µm for a single lens surface. Accordingly, one would expect to measure a valley depth of approximately 1 µm for a bi-concave lens. However, only a valley depth of about 0.2 µm is observed in Fig. 4(g). Although not all 60 lenses were measured by in-lab metrology individually, we speculate that the shape profile measurements by the LSM are not reliable to accurately describe induced wavefront errors revealed by the X-ray measurements, as the LSM has limited capability in measuring steep slopes and only offers a stated height accuracy of 1.4 µm when measuring lenses with a depth of 120 µm. In Addition, the derived shape error by the X-ray measurements are averaged values, which may deviate significantly from the single lens error.
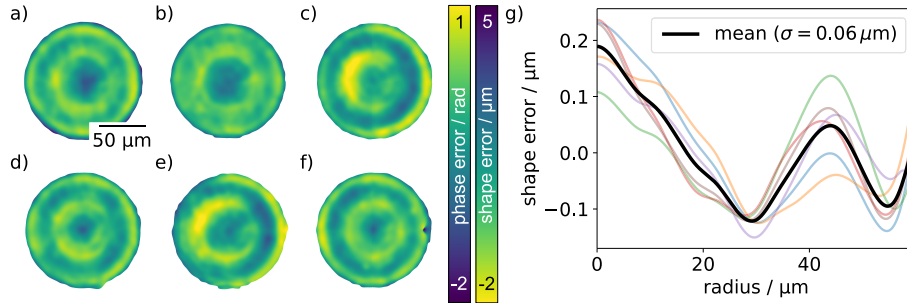

Fig. 4. Residual wavefield error in the plane of the lens stack exit and derived shape error. a) - f) Wavefield error of LC 1 to 6 with 10 lenses in each cube at 9 keV. The scale bar in a) is shared among others. g) Derived single lens error. The RMSE of the mean shape is 0.06 µm.

The phase plate structure was determined by directly converting the non-radially symmetric two-dimensional phase error maps shown in Fig. 4(a) to (f) into a height-based shape error map by Eq. (1), indicating that the height of the phase plate structure is below 7 µm. These structures were implemented on 6 diamond substrates, sourced from the same lot as the lenses, using laser ablation. The substrates were thinned down to an averaged thickness of 35.5 µm before implementing the phase plate structures on them. In this way, 6 individual phase plates were fabricated for each corresponding stack of 10 lenses.

5. Implementation of the aberration-corrected lens cubes

As a scanning hard X-ray microscope designed for sub-100 nm spatial resolution, the PtyNAMi instrument has certain constraints for X-ray optics integration, as depicted in Fig. 5. Specifically, the stages responsible for holding and moving attached optics have constraints in terms of load capacity and travel range, which restrict the weight and working distance of the optics. The

instrument typically operates with focusing optics such as nanofocusing lenses (NFLs) and multilayer Laue lenses (MLLs) [16], indicating that it is generally designed for creating focal spots smaller than 100 nm and focal length shorter than 30 mm. Additionally, the lens aperture needs to be adjusted to match the lateral coherence length for coherent scanning applications such as ptychography, which in the horizontal direction is typically smaller than 140 µm. The focal length must be within certain limits and the lens configuration must be flexible enough to meet that focal length for a wide energy range. To adapt diamond lenses for use with this instrument, the aforementioned concept involving intrinsically-aligned and aberration-compensated LCs suitable for various photon energies offers an excellent solution.
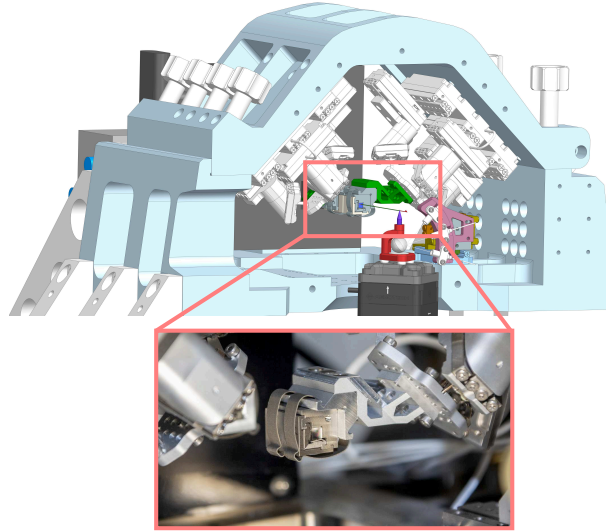

Fig. 5. PtyNAMi experiment setup at nanoprobe endstation of P06 of PETRA III. For the evaluation of the concept, two LCs containing 20 and 40 diamond lenses, respectively, alongside their corresponding phase plates, as shown in Fig. 2(b), were mounted in series onto the optics stage of the PtyNAMi setup.

To evaluate this concept, 6 sets of 10 diamond lenses were assembled in two larger LCs, containing 20 and 40 diamond lenses, respectively. Initially, the LCs were measured without phase plates. Subsequently, dedicated phase plates were installed after each 10 lenses within the LCs, as shown in Fig. 2(b). The order in which the lenses are assembled corresponds to the order in which they were arranged within each 10-lenses set during characterization, described earlier in Section 4.2. In this configuration, the 10-lenses LC in Fig. 3 are replaced by the combined LCs as shown Fig. 2(b) and in the lower photo of Fig. 5. Two spring clips are used to fix two LCs in an aluminum holder, respectively. The distances between the LCs and the sample, as well as between the sample and the detector, are provided in Table 1 with corresponding photon energy. A squared area of 2 µm × 2 µm of the Siemens star was raster scanned in a regular grid pattern with a 50 nm step size and a dwell time of 0.1 s per point. Figure 6(a) shows the measured wavefront error at the exit of the LCs without phase plates at 14 keV as an example. The RMSE of the phase is 1.16 rad. The wavefront error with integrated phase plates for the LCs is shown in Fig. 6(b) for direct comparison. A reduction in wavefront RMSE down to 0.65 rad is achieved. Figure 6(c) shows a comparison of the radially integrated phase error around the center of the wavefront error map at all three measured photon energies. Here, the phase plates clearly lead to an improvement, reducing the RMSE of the radially integrated phase from 0.78 rad to 0.32 rad at 17 keV and from 0.98 rad to 0.14 rad at 20 keV. The position shift of peaks and valleys in the plot

of uncorrected wavefront reflects the different beam convergence inside the optically thick lens stack at different photon energy.
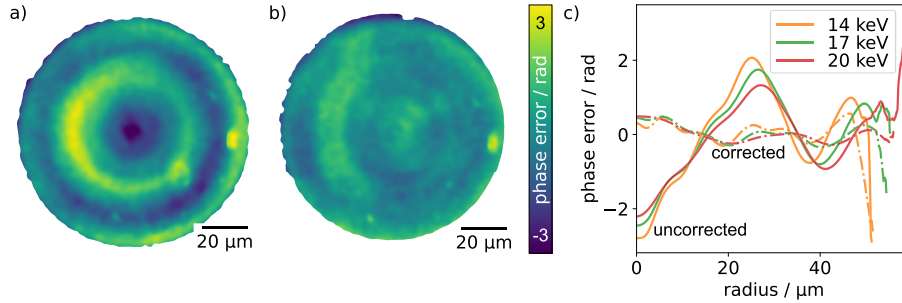

Fig. 6. Comparison of wavefront error. a) Wavefront error at the exit of the lens stack without phase plates at 14 keV. b) Wavefront error at the exit of the lens stack with phase plates at 14 keV. c) Radially integrated wavefront error for both cases at different photon energies.
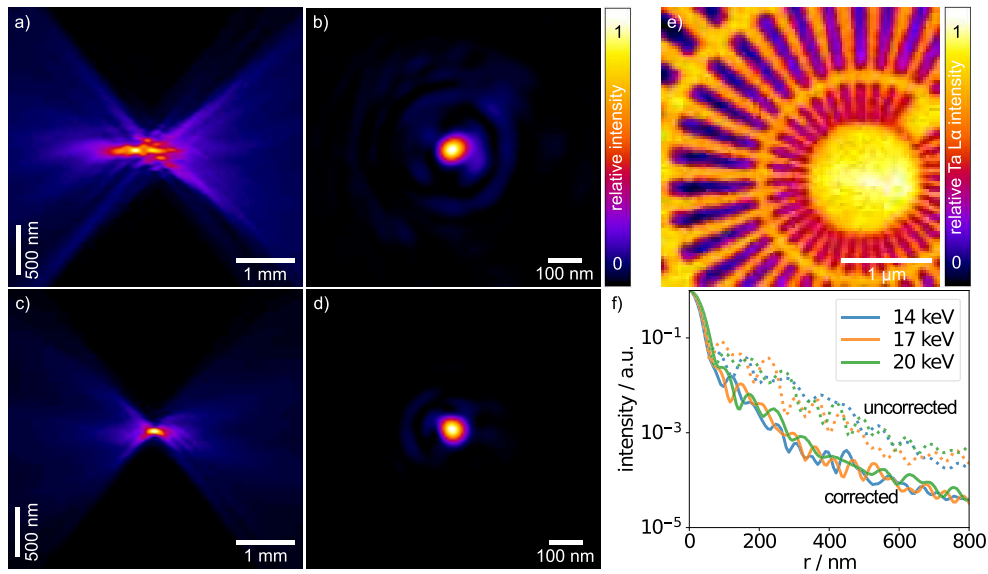

Fig. 7. Beam profile and focus quality of the combined LCs, containing 20 + 40 = 60 diamond lenses, without and with phase plate at 14 keV. a) Beam caustic without phase plate. b) Focus spot intensity without phase plates. c) Corrected beam caustic. d) Focus cross intensity with phase plates. e) 2D-XRF image obtained by measuring Ta Lα fluorescence lines while scanning the Siemens star. f) Radial focus profile at different photon energies.

The impact of using phase plates on the beam shape and focal spot characteristics is highlighted in Fig. 7. Using results at 14 keV as example again, the beam caustic in vertical direction for the LCs without phase plates is shown in Fig. 7(a). The phase error leads to tails and a second focal spot on the upstream side of the focus, which are clear signatures of spherical aberrations. For the LCs with phase plates shown in Fig. 7(c), the tails and second focal spot vanished, indicating significant improvements. The LCs without phase plates created a focal spot of 62 nm × 53 nm full-width at half-maximum (FWHM), shown in Fig. 7(b), with some side lobes and intensity rings around. An improvement of the focal spot size to 52 nm × 51 nm FWHM is achieved with

phase plates, and side intensity is barely visible, as shown in Fig. 7(d). The reached focal spot size is comparable with theoretical values listed in Table 2. The scanned X-ray fluorescence image of the resolution test sample made by NTT-AT (ATN/XRESO-50HC) further proves this with the 50 nm smallest features being clearly resolved, as shown in Fig. 7(e). The radially integrated intensity distribution around the center of the focal spot, plotted in Fig. 7(f) for all three photon energies, confirms a reduction of intensity in the first side ring by an order of magnitude. The fraction of the total intensity that is concentrated in the central focal spot is expressed by the Strehl ratio. Here, we calculate the Strehl ratio by comparing the intensity in the central speckle of the focus with numerical simulation of a lens system with identical parameters. It improved from 0.32 to 0.69 for 14 keV, which indicates a reduction in residual intensity outside the central focal spot by a factor of 2.2.

Table 2. Summary of the performance for the combined diamond lens, consisting of 60 lenses in total, separated into two LCs containing 20 and 40 lenses, respectively. Photon counts were measured by integrating the EIGER detector images and taking the quantum efficiency of the detector [23] into account. WD refers to the working distance, PP denotes the phase plate, and T represents the initial transmission measurements, while the values in brackets are results from the subsequent energy scan measurements.

E (keV)	WD (mm)	PP	Focus H × V (nm)	Diffraction limit H × V (nm)	Strehl ratio	T (%)	Theor. T (%)	Photon counts (s^{-1})
14	49.6	no	62 × 53	49 × 49	0.32	—	—	—
		yes	52 × 51		0.69	25 (28)	26	9.15×10^8
17	76.2	no	56 × 50	56 × 56	0.26	—	—	—
		yes	57 × 57		0.75	36 (39)	40	8.82×10^8
20	108.1	no	65 × 58	64 × 64	0.35	—	—	—
		yes	67 × 68		0.83	34 (46)	49	4.26×10^8

Table 2 provides a summary of the performance metrics for the LCs, both with and without integrated aberration correction, across three different photon energies. The working distances for these photon energies fall within the operational constraints of the PtyNAMi instrument. The LCs can also be implemented separately to suit various applications. The focal spot sizes are all very close to the theoretical values. Notably, the enhancement in the Strehl ratio across the three photon energies, facilitated by phase plates, is substantial. At photon energies of 17 and 20 keV, the FWHM focus size of the lens stack without phase plates is marginally smaller than that with phase plates and is even smaller than the diffraction limit. Considering the multiple focal spots observed in Fig. 7(a) which suggest that the X-rays were focused by different ring-shaped regions of the lens stack, this effect may be attributed to the ring-shaped illumination which can lead to focal spot beyond the diffraction limit for a circular aperture [21]. The theoretical transmission was calculated by taking the absorption in air and in the phase plates into account. Initial transmission measurements at selected photon energies were obtained by comparing the downstream PIPS diode signals recorded with and without the lenses in place. However, the transmission at 20 keV was significantly lower than the theoretical value, possibly due to a specific alignment angle of the combined LCs, resulting in a so-called 'X-ray glitch' or 'diffraction loss' well-known in X-ray spectroscopy [22]. Therefore, additional measurements were carried out by performing an energy scan from 14 keV to 20 keV in 10 eV steps with a fixed LC alignment, while simultaneously recording data from the downstream PIPS diode and an upstream ionization chamber, which was placed between the entrance pinhole and the LCs. The energy scan was repeated twice, once with the LCs installed and once without the LCs. The aperture pinhole was present in both measurements. The PIPS diode signals were normalized to the ionization chamber to eliminate potential effects of beam intensity fluctuations. Figure 8 shows the corresponding

transmission measurement results, indicating a transmission close to the theoretical values. We suspect that the fluctuations in transmission, especially at higher energies, are due to an increasing likelihood of single diamond grains getting into diffraction condition. These findings affirm that the concept of assembling multiple LC packages, comprising varying quantities of diamond lenses and corresponding phase plates, is effective in enabling versatile applications across a wide range of photon energies, while delivering high-quality focusing performance.
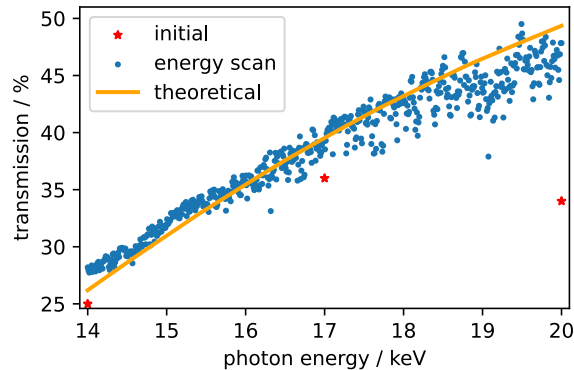
Fig. 8. Measured and theoretical transmission of the combined LCs over a photon energy range from 14 keV to 20 keV. Blue points are results of energy scan measurement while red stars refer to the results of initial measurements at 14, 17 and 20 keV.

6. Conclusion

The results presented highlight the successful fabrication of high-quality diamond refractive X-ray optics using femtosecond laser ablation at DESY, along with the development of an X-ray lens cube (LC), featuring integrated aberration compensation and intrinsic alignment capabilities. Using a total of 60 lenses with a radius of curvature $R = 25$ μm and dedicated phase plates for every 10 lenses, this concept has been demonstrated on the PtyNAMi instrument across a wide range of photon energy below 20 keV, delivering aberration-minimized focal spots close to the diffraction limit. Remarkably, this marks the first time that diamond lenses have achieved a focus size of approximately 50 nm. Furthermore, the two lens packages have been successfully deployed as operational user optics at beamline P06. For other applications utilizing standard CRL holders, these diamond LCs can also be easily integrated.

References
1. C. G. Schroer, M. Kuhlmann, U. T. Hunger, *et al.*, "Nanofocusing parabolic refractive x-ray lenses," Appl. Phys. Lett. **82**(9), 1485–1487 (2003).
2. S. Terentyev, V. Blank, S. Polyakov, *et al.*, "Parabolic single-crystal diamond lenses for coherent x-ray imaging," Appl. Phys. Lett. **107**(11), 111108 (2015).
3. L. Wei, P. K. Kuo, R. L. Thomas, *et al.*, "Thermal conductivity of isotopically modified single crystal diamond," Phys. Rev. Lett. **70**(24), 3764–3767 (1993).

4. T. Roth, L. Alianelli, D. Lengeler, *et al.*, "Materials for x-ray refractive lenses minimizing wavefront distortions," MRS Bull. **42**(06), 430–436 (2017).
5. O. Chubar, L. Wiegart, S. Antipov, *et al.*, "Analysis of hard x-ray focusing by 2D diamond CRL," in *Advances in Computational Methods for X-Ray Optics V*, K. Sawhney and O. Chubar, eds., (SPIE, 2020), p. 20.
6. S. Terentyev, M. Polikarpov, I. Snigireva, *et al.*, "Linear parabolic single-crystal diamond refractive lenses for synchrotron X-ray sources," J. Synchrotron Radiat. **24**(1), 103–109 (2017).
7. S. Antipov, S. V. Baryshev, J. E. Butler, *et al.*, "Single-crystal diamond refractive lens for focusing X-rays in two dimensions," J. Synchrotron Radiat. **23**(1), 163–168 (2016).
8. R. Celestre, S. Antipov, E. Gomez, *et al.*, "Polished diamond X-ray lenses," J. Synchrotron Radiat. **29**(3), 629–643 (2022).
9. L. Xue, H. Zhang, Y. Wang, *et al.*, "Analysis of the impact of misalignments bi-concave diamond lens on wavefront," Nucl. Instrum. Methods Phys. Res., Sect. A **1073**, 170282 (2025).
10. F. Seiboth, A. Schropp, M. Scholz, *et al.*, "Perfect X-ray focusing via fitting corrective glasses to aberrated optics," Nat. Commun. **8**(1), 14623 (2017).
11. F. Seiboth, F. Wittwer, M. Scholz, *et al.*, "Nanofocusing with aberration-corrected rotationally parabolic refractive X-ray lenses," J. Synchrotron Radiat. **25**(1), 108–115 (2018).
12. F. Seiboth, D. Brückner, M. Kahnt, *et al.*, "Hard X-ray wavefront correction via refractive phase plates made by additive and subtractive fabrication techniques," J. Synchrotron Radiat. **27**(5), 1121–1130 (2020).
13. V. Dhamgaye, D. Laundy, S. Baldock, *et al.*, "Correction of the X-ray wavefront from compound refractive lenses using 3D printed refractive structures," J. Synchrotron Radiat. **27**(6), 1518–1527 (2020).
14. F. Seiboth, A. Schropp, M. Lyubomirskiy, *et al.*, "On-chip aberration correction for planar nanofocusing x-ray lenses by focused ion-beam milling," Appl. Phys. Lett. **122**(24), 241105 (2023).
15. C. G. Schroer and B. Lengeler, "Focusing hard x rays to nanometer dimensions by adiabatically focusing lenses," Phys. Rev. Lett. **94**(5), 054802 (2005).
16. A. Schropp, R. Döhrmann, S. Botta, *et al.*, "PtyNAMi: ptychographic nano-analytical microscope," J. Appl. Crystallogr. **53**(4), 957–971 (2020).
17. A. Schropp, P. Boye, J. M. Feldkamp, *et al.*, "Hard x-ray nanobeam characterization by coherent diffraction microscopy," Appl. Phys. Lett. **96**(9), 091102 (2010).
18. F. Seiboth, M. Kahnt, M. Scholz, *et al.*, "Quantitative characterization of aberrations in x-ray optics," in *Advances in X-Ray/EUV Optics and Components XI*, A. M. Khounsary, S. Goto, and C. Morawe, eds. (SPIE, 2016), p. 99630P.
19. F. Pfeiffer, "X-ray ptychography," Nat. Photonics **12**(1), 9–17 (2018).
20. I. Johnson, A. Bergamaschi, H. Billich, *et al.*, "Eiger: a single-photon counting x-ray detector," J. Instrum. **9**(05), C05032 (2014).
21. T. Breen, N. Basque-Giroux, U. Fuchs, *et al.*, "Tuning the resolution and depth of field of a lens using an adjustable ring beam illumination," Appl. Opt. **59**(15), 4744–4749 (2020).
22. D. Chen, J. Dong, X. Zhang, *et al.*, "Suppression of Bragg reflection glitches of a single-crystal diamond anvil cell by a polycapillary half-lens in high-pressure XAFS spectroscopy," J. Synchrotron Radiat. **20**(2), 243–248 (2013).
23. T. Donath, D. Šišak Jung, M. Burian, *et al.*, "EIGER2 hybrid-photon-counting X-ray detectors for advanced synchrotron diffraction experiments," J. Synchrotron Radiat. **30**(4), 723–738 (2023).